

<sup>1</sup> Masters Thesis: The Evolution of Fault Slip Surfaces with  
<sup>2</sup> Cumulative Displacement

<sup>3</sup> Kelian Dascher-Cousineau

<sup>4</sup> January 27, 2017

<sup>5</sup> **Abstract**

Fault slip surface roughness determines fault strength, friction and dynamic fault processes. Wear models and field observations suggest that roughness decreases with cumulative displacement. However, measurements have yet to isolate the effect of displacement from other possible controls, such as lithology or tectonic setting. We present an unprecedentedly large fault surface dataset collected in and around the San-Rafael Desert, S.E. Utah, United States. In the study area, faults accommodated regional extension at shallow 1 to 3 km depth and are hosted in the massive, well sorted, high porosity Navajo and Entrada sandstones. Existing detailed stratigraphic throw profile provide a maximum constraint for displacement. Where cross-sectional exposure is good, we measure exact displacement imparted on slip surfaces using offset in marker horizons. Thereby, we isolate for the effect of displacement during the embryonic stages of faulting (0 to 60 m in displacement). Our field observations indicate a clear compositional and morphological progression from isolated joints or deformation bands towards smooth, continuous and mirror-like fault slip surfaces with increasing displacement. To quantify these observations, slip surfaces were scanned with a white light interferometer, a laser scanner and a ground based Lidar. Together these instruments resolve more than eight decades of spatial bandwidth (from less than  $\mu\text{m}$ 's to m's in scale). Preliminary results indicate that roughness decreases with displacement according to a power law. Roughness measurement associated with only maximum constraints on displacements corroborate this result—for a given displacement, minimum roughness is bounded by the later smoothing trend. In addition, we find that the maximum roughness is fixed—bounded a by a primordial roughness corresponding to that of joints surfaces and deformation band edges. Our results build towards a coherent model of fault wear robust to ambiguities associated to displacement estimates, spatial scaling and geological context.

<sup>30</sup> *Will have to include relationship to white light data, modelling results/interp*

<sup>31</sup> **Contribution of Authors**

<sup>32</sup> **1 Introduction**

<sup>33</sup> Would closely follow my project proposal:

<sup>34</sup> **1.1 Motivation**

<sup>35</sup> Faults are a characteristic feature of the Earth's brittle crust. Fluid flow, seismicity and crustal  
<sup>36</sup> mineralization are just few systems upon which faults act as major controls (Sibson, 1977). In  
<sup>37</sup> spite of their importance, some aspects of faults and their underlying processes remain poorly

understood. How strong is a fault? How do faults mature? Are small faults mechanically different to large faults? Fault geometry has been shown to be a key parameter controlling the mechanical behavior and evolution of faults (e.g. Lay et al., 1982; Aki, 1984; Power et al. 1988; Chester and Chester, 2000), but these questions are not yet fully answered.

Slip on a fault occurs on discrete slip surfaces in fault zones (Davatzes and Aydin, 2005). These surfaces are not planar; they are rough. Roughness is observable at all scales (Scholtz and Aviles, 1986; Candela et al., 2012). Slickenlines, corrugations, mullions and jogs are all surface features that can be seen at different length scales (Sagy and Brodsky, 2009). Field studies have found common characteristics in the topography of fault surfaces. These can be summarized as follows: 1) Fault surfaces appear to be well defined by large fractal domains, wherein 2) faults are smoother at larger length scales (Scholtz and Aviles, 1986; Candela et al., 2012), 3) rougher in the slip perpendicular direction than in the slip parallel direction (Lee and Bruhn, 19960, and 4) slip surfaces are smoother with cumulative displacement (Sagy et al., 2007). Fault roughness has been demonstrated to be critical in determining the strength (Chester and Chester, 2000, Brodsky et al., 2016), triggering (Parsons, 2008), dynamic properties (Candela et al., 2011; Dunham et al., 2011), spatial distribution (Parson, 2008) and failure recurrence of faults (Stirling et al., 1996). It is increasingly evident that roughness is a fingerprint of fundamental features of the faulting process (Brodsky et al., 2016). In accordance, incorporating more complex sources geometries has become a more frequent practice in dynamic earthquake rupture modelling (Shi and Day, 2013; Dunham et al., 2011).

Changes in roughness, as determined by cumulative displacement (Sagy et al, 2007; Brodsky et al, 2011), imply faults mature. Fundamental differences between immature and mature fault have far-reaching implications. Fixed source parameter scaling of earthquakes is a pillar of earthquake seismology. However, analysis of seismic signals of immature faults vs. mature faults suggest that scaling is sensitive to cumulative displacement. This observation leads to an interpretation of fundamental differences in earthquake populations. Specifically fault maturation would undermine the applicability of a constant magnitude scaling. Evolving mechanical properties such as fault friction and static strength—both associated to fault roughness—would imply that immature and mature faults belong to distinct populations with distinct scaling. (Harrington and Brodsky, 2011)

While there has been significant progress in understanding the role of roughness in the faulting process, how and why fault surfaces change is still unclear (e.g. Candela et al., 2011; Dunham et al., 2011; Brodsky et al., 2016). Sagy et al. (2007) noted a systematic decrease in roughness of ‘mature’, large displacement faults compared to ‘immature’ faults with low displacements. Similar results have since been observed along reactivated joints, in laboratory experiments (Davidesko et al., 2014), and in compilations of fault roughness analysis (Brodsky et al., 2011; Candela et al., 2012). These studies all attribute the decrease in roughness to wear at the fault interface. However, these data show only weak correlations between fault roughness and cumulative displacement. Indeed, relating roughness and cumulative displacement is not trivial. Fault surfaces in exhumed faults are rarely well preserved. Furthermore, obtaining well-constrained displacement estimates is contingent on the presence of precise and accurate kinematic indicators. Combining observations over a broad range of displacements is challenging. Consequently, it is unclear whether trends observed in compilations of roughness measurements from multiple faults are directly attributable to displacement or a combination other geological factors. For instance, while comparing fault surfaces from geologically diverse datasets, variations in lithology, faulting mechanism, temperature and depth may all be introducing further systematic variations.

Additionally, the evolution of roughness represents a novel insight into the architecture of a fault zone. The geometry of the fault surface modulates the architecture of the whole fault zone (Mitchell and Faulkner, 2009). Changes in roughness require interaction between the slip

surfaces and its direct surrounding (fault core), resulting in the formation of fault rock (Power and Tullis, 1988). In addition to earthquake mechanics, the architecture of a fault zone, and its corresponding permeability structure, is very important for hydrocarbon exploration (Shipton and Cowie, 2003). However, because the change in roughness by wear is poorly understood, the equivalent production of wear material, the fault rock, is also poorly understood. Fault rock thickness growth with displacement is documented (Sholtz, 1987), but variability is such that even order of magnitude estimates of thickness for a given displacement are unavailable.

The objective of this project is to identify how and why fault surfaces change. In line with previous studies, I hypothesize that wear is a dominant mechanism in the evolution of fault surfaces with cumulative displacement. I will measure the surface roughness of natural fault surfaces with varying displacements to confirm and better quantify the role of cumulative displacement on fault roughness. This study will be broadly composed of the following three components: 1) data collection, 2) data processing and analysis and 3) interpretation of the results. Field work in Southern Utah will be conducted with the specific intent of collecting scans of pristine fault surfaces with terrestrial laser scanners and hand-samples for laboratory high resolution scans. The roughness of the surfaces will then be quantified and related to corresponding displacement. A robust quantitative correlation between roughness and cumulative displacement will enable parameterized interpretation and modelling of the mechanics of fault wear. Based on my results, I will explore the mechanical implications of a changing fault surface as coupled to the fault zone. In this proposal, I first present the geological background and important concepts. I then follow by outlining the projected scientific method, data analysis and interpretation. I conclude with a time line for the completion of my thesis in a timely two year period.

## 1.2 Fault Roughness

The deviation from planarity formally defines roughness (Brown and Scholz, 1985). Pioneering studies used contact profilometers to measure the roughness of fault surfaces (Scholz and Aviles, 1986; Power and Tullis, 1991. Combined with surface profiles of large scale continental faults, faults were found to have a remarkably broad fractal band ranging over 10 orders of magnitude—from  $10^{-5}$  to  $10^5 m$  (Scholz and Aviles, 1986). Over these length scales, fractal scaling is said to be statistically self-affine. A statistically self-affine profile along  $x$  with heights  $h(x)$ , is invariant under the affine transformation:

$$\begin{cases} x \rightarrow \lambda x \\ h \rightarrow \mu h \end{cases} \quad (1)$$

This relation therefore implies an exponential relation between the scaling,  $\lambda$  (along  $x$ ), and  $\mu$  (along  $h$ ) such that:

$$\mu = \lambda^\varsigma \quad (2)$$

Where  $\varsigma$  is a constant named the Hurst exponent. Note that self-similarity, is an instance of self-affinity where the Hurst exponent is 1 (Schmittbulh et al., 1993). Developments in laser scanner technology over the past decade, particularly terrestrial laser scanners, allowed surfaces to be characterized by calculating the Hurst exponent from thousands of cross sectional profiles through a fault surface (e.g. Candela et al., 2012). Studies of natural mode I crack surfaces have observed self-affinity with a Hurst exponent of  $\sim 0.8$  at all scales of observation (Scholtz, 1985). Shear, or mode II cracks (i.e. faults) are different. They are anisotropic—the Hurst exponent parallel to shear ( $\sim 0.6$ ) is smaller than that in the shear-perpendicular direction ( $\sim 0.8$ ) (Lee and Bruhn, 1996).

Another parameter is required to fully describe surface roughness. While the Hurst exponent describes the scaling behavior of the roughness it does not define the magnitude of the roughness. The pre-factor defines the amplitude of the scaling law (Candela et al., 2009). The pre-factor is subject to significant variation. Overall, observations show that fault surfaces have distinctly smoother profiles along slip direction than perpendicular to slip (Lee and Bruhn, 1996). Many methods exist to quantify roughness scaling, possibly most intuitive of which is the Root Mean Squared (*RMS*) as a function of scale. For a profile of length  $L$  with a point spacing of  $\Delta x$  with deviation  $h$  from the best fit line, the *RMS* for a given scale  $s$  is defined as follows:

$$RMS(s) = \sqrt{\frac{\Delta x}{L} \sum_{i=1}^{L/\Delta x} h_i^2} \quad (3)$$

The *RMS* roughness of a fault or fracture exhibits power-law scaling with segment length. A self-affine profile should therefore plot as a straight line on a log-log plot of the *RMS* as a function of the segment length with a slope equivalent to the Hurst exponent. (Schmittbuhl et al., 1993) The power spectrum of a surface profile has been shown to yield more robust roughness metrics (Schmittbuhl et al., 1993; Candela et al., 2009). For a set of discretely sampled points, the power spectrum of a profiles is the result of a Fast Fourier Transform (FFT). The spectrum defines the surface profile as superposition of sinusoidal profiles. In the frequency domain, rougher profiles will have correspondingly higher amplitudes, or power. The power spectrum,  $P(k)$ , of a self-affine profile (again in log-log space) defines a line as follows:

$$P(k) = Ck^{(-1-2\zeta)} \quad (4)$$

Where  $k$  is the frequency and  $C$  is the pre-factor (Candela et al., 2009).

### 1.3 Wear

### 1.4 The evolution of slip surfaces with displacement

*talk about deformation in sandstones, e.g. aydin, fossen etc.*

In this project, I hope to address how slip surfaces change. Many processes could cause the slip surface to change. In fact, the cause of change to the slip surface is not uniquely recorded by the roughness. Fundamentally, a fault surface can only change according to the following mechanisms:

*Addition of material*

*Redefinition of the slip surface by fracture*

*Removal of material*

I have hypothesized that the change in surface roughness is the result of wear—an instance of removal of material. As fault blocks slide past each other, frictional wear is an inevitable process. Layers of comminuted fault rock are direct evidence of this process (Power and Tuillis 1988). Wear is the subject of a vast field of research, particularly in engineering and tribology due to interest in lubricating and manufacturing machine parts for longevity (Meng and Ludema, 1995). Here, I outline only basic wear mechanics (i.e. Archard, 1953). Wear is formally defined as frictionally induced volume removal from surfaces in sliding contact. The wear rate, the amount of wear per unit distance is broadly related to the real area of contact and loading. When two surfaces are put in direct contact, the real area of contact is much smaller

than the nominal surface areas because the load is supported at microscopic protrusions from a surface, called asperities. Remote loading normal to the surface causes local stresses and associated deformations at contact points. Note that as the load is increased, deformation of large asperities causes new asperities to come in contact. In its simplest form, wear rate defined as:

$$W \propto \frac{P}{a} \quad (5)$$

Where  $W$  is the wear rate,  $P$  is the remote load and  $a$  is a mean measure of the dimensions of the asperities in contact during sliding. The relation has been shown to be reasonably robust in experimentation for most materials. In further detail, the size, distribution and duration of contact areas, as well as the shape of the worn particles, control the general behavior of wear. Note that material properties are implicitly buried in a probability factor—the probability of a collision of asperities to lead to removal of material (Archard, 1953). If and how wear affect the geometry of a fault slip surface remains unclear. Both field and laboratory experiment show that wear is scale dependent, such that asperities are worn down at different rates according to their typical dimensions. Asperities at longer characteristic wavelengths and larger amplitudes wear down faster, on average, than those with small wave lengths and small amplitudes. These observations correspond to both a downward translation and clockwise rotation of the self-affine scaling in the power spectrum. The exact mechanism causing this behavior is unclear. Davidesko et al., 2014 suggest that dilation during displacement on a fault ‘shelters’ smaller, shorter wavelength, asperities and therefore wears down large, long wavelength asperities. In this study, I hope to be able to relate changes in the slip surface geometry to wear processes. Specifically, empirically identifying and determining the rate of wear as expressed in the slip surface would be of particular interest. A potential caveat to the simple wear models (i.e. Archard, 1953) is the sensitivity of fault rock to sliding velocity and the presence of lubricant (e.g. pseudotachylyte, amorphous silica gel and gouge). Moreover, the stresses imparted by a propagating fault rupture front are mechanically distinct from those related to rubbing surfaces. Such a distinction may also drastically alter the relation between wear material and the slip surface (Sibson, 1977). Since Archard (1953), models of wear tend to diverge in their results, assumptions and by association, their applicability (Meng and Ludema, 1995). For the purpose of this study, the fractal nature of fault surfaces is important to reconcile with a model of wear. What is the scaling behavior of wear? Fractal surfaces are difficult to integrate into the pre-existing framework of wear processes. Specifically, defining the real area of contact, corresponding deformation and, by association, the scale dependence of wear is non-trivial (e.g. Persson, 2001; Jackson and Streator, 2006).

## 2 Geology

*maybe put as a separate section (like 2)*

Field work will be conducted in the San-Rafael Desert, Utah (see figure 1). The San Rafael Desert hosts a sequence of gently dipping marine and sub-areal sedimentary rocks deposited from the Pennsylvanian to the Jurassic (see Figure 2). The San Rafael Desert is part of the San Rafael Swell, a monocline that formed when these sediments were uplifted as a passive drape fold above a reactivated basement reverse fault during the Late Cretaceous Laramide Orogeny (Kelly, 1955; Vrolijk et al., 2005). The swell is part of the broader Colorado Plateau (Kelly, 1955). Networks of joints and normal faults associated to further Laramide activity cross-cut sedimentary sequence accommodating North-South extension (Aydin and Johnson, 1978; Vrolijk et al., 2005). Specifically, within the San Rafael Swell we have selected the following field locations: 1) the Chimney Rock Fault Array, 2) the Big Hole fault and 3)

a network of deformation bands in the Entrada formation near Goblin Valley State Park. Advantages of these field locations are manifold. First, the nearly pure quartzite lithology, extensional tectonic regime, depth (2-4 km or 40-80 MPa), temperature (estimates range from 45-90 oC) of activity, and faulting mechanism are all relatively consistent (Vrolijk et al., 2005). Consistency in these parameters is key to isolating the effect of displacement on the fault roughness. Moreover, both field locations exhibit well preserved fault surfaces that are exposed and accessible (see Figure 3). The Chimney Rock fault array is an orthorhombic set of faults that crops out at the northern end of the San Rafael Swell (Krantz, 1989, Davatzes et al., 2003). Two pairs of oppositely dipping normal faults crop out at the surface with preserved fault scarps. WNW-striking faults are interpreted to have formed by shear reactivation of joints, whereas ENE-striking faults initially formed from deformation bands (Davatzes, 2003). Exposure is very good, faults are abundant and have well preserved fault surfaces (Vrolijk et al., 2005). The Chimney fault array has studied to better understand of fault geometry (Shipton and Cowie, 2001; Shipton and Cowie, 2003), permeability (Shipton et al., 2002) and kinematics (Krantz, 1986; Krantz, 1989; Maerten et al., 2001; Davatzes et al., 2003) . As a result, detailed maps of the fault array have been produced (e.g. Maerten et al., 2001) . In addition, by using measurements of the separation between footwall and hanging wall cutoffs of sedimentary horizons, entire displacement profiles have been measured for faults with a wide range of displacements (Cowie and Shipton, 1998; Maerten et al., 2001; Shipton and Cowie 2001; Shipton and Cowie, 2003). The Big Hole fault is located just to the South-East of the Chimney Rock Fault Array. While not explicitly part of the fault array, the Big Hole fault shares a nearly identical geological setting. The Big Hole fault has been extensively studied in detail as an analog to hydrocarbon reservoir-scale faults. Displacements on the exposed fault range from 8 m to 39 m. (Shipton and Cowie, 2001; Shipton and Cowie, 2003) Large networks of deformation band faults outcrop near Goblin Valley State Park on the southeastern margin of the San-Rafael Swell (Aydin and Johnson, 1978). Deformation bands are the result of concentrated shear deformation on narrow centimeter thick bands (Aydin and Johnson, 1978; Davatzes et al., 2003). Collapsing pore space accommodates this deformation. Deformation bands are interpreted as the embryonic stages of fault development (Fossen and Hesthammer, 1998; Fossen et al., 2007). Because deformation bands dramatically alter the local permeability structure, Goblin Valley has been extensively studied in light of fault nucleation and the implications for hydrocarbon circulation (e.g. Fossen et al., 2005; Tobari and Fossen 2009). At Goblin valley, arrays of deformation bands anastomose—outcropping as centimeter- to meter-sized slabs. These are often bounded by discrete slip surfaces with well-preserved striations — i.e. roughness (Aydin and Johnson, 1978). Offsets in sedimentary beds have allowed previous studies to obtain detailed displacement measurements (e.g. Schultz and Fossen 2002). Together, these field locations offer the chance to survey well-preserved fault surfaces that have hosted displacements from embryonic stages to 30 m of displacement. Moreover, novel to this study, we will be able to survey multiple expressions of a single fault's surface with various displacements according the displacement profile of the fault.

### 3 Method

This study focuses on the qualitative and quantitative evolution of fault slip surfaces—both addressing how fault slip surfaces evolve and the implications thereof. The quality of the displacement measurements and the large number of accurate surface scans are fundamental to the quantitative analysis of the data. Field-method and data acquisitions thus reflect these standards.

For the qualitative analysis, we carefully record the characteristics of the fault architecture in the context of fault evolution. Specifically, we are particularly meticulous about 1) identifying

261 cross-cutting relationships which indicate temporal evolution on the on fault, 2) identifying the  
262 evolutionary stages in the formation of faults and 3) identifying and characterizing the wear  
263 product, or fault rock, produce as faults evolve.

264 For the quantitative analysis, we collect scans both *in situ* and from hand samples collected  
265 in the field. Scans are associated to a constraint on displacement. Moreover, for every scan,  
266 the time of day, location, quality, strike and dip of the fault slip surface as well as the rake of  
267 the slickenlines are recorded. When possible we record an estimate of the fault rock thickness.  
268 Finally, we also record both a plan and cross-sectional view image of the scanned fault surfaces.  
269 See appendix for the tabulation of this data. Together, all these measurements and observations  
270 should provide the necessary data to robustly explain and quantify the process through which  
271 faults mature.

### 272 3.1 Scan Data Acquisition

273 To measure slip surface roughness we analyses large point clouds scans of real fault surfaces and  
274 average the slip parallel and perpendicular spectral and statistical properties across hundreds  
275 of profiles. Point clouds must be obtained across a flexible array of instruments to properly  
276 capture the fractal scaling behavior (Brown and Scholtz, 1985; Candela et al., 2012). In this  
277 study, we use three instruments with complimentary scales of observation. Together, these  
278 instruments offer accurate and precise three-dimensional discretization of fault surfaces at over  
279 nine decades of length scale.

280 \*make a map of each areas with the location of every scan encoded with different symbols\*

281 At the largest scales ranging from meters down to millimetres, a light detection and ranging  
282 instrument (i.e. LiDAR). We use the LiDAR has been used in many previous studies of fault  
283 roughness as it is easily deployable in the field and provides rapid means to collet very large point  
284 cloud data set. However, its use is limiting as it requires exceptionally good and, accordingly,  
285 rare exposure of fault surfaces that are large enough and fresh enough to not have been degraded  
286 by erosion. In this study, we report 5 ??? Lidar Scans (see figure).

287 Instead, the bulk of *in situ* field measurements were made at intermediate scales ranging  
288 from centimeters down to hundreds of microns with the NextEngine 3D laser scanner. The  
289 NextEngine laser scanner is accurate down to 100 microns with resolution up to 41 540 points  
290 per square centimeter. Note that the NextEngine is a much less cost prohibitive option when  
291 compared to the LiDAR yet captures the same characters of the fault surfaces. The laser  
292 scanner was benchmarked to a machined-flat granite surface and to a scan of the corona slip  
293 surface both to industrial-grade laser scanner as reference. The scanner is not exactly built to  
294 be field ready. It requires a power source, low light conditions, a stable surface to sit on, limited  
295 dust exposure and must be connected to a computer. Moreover it only allows for a very limited  
296 depth of field. To use the scanner in the field, we connected both the laser scanner and laptop  
297 to a solar powered, *goal zero*, battery. The scanner was encased and padded in a reinforced  
298 cardboard box with its depth exactly equivalent to the optimal depth of field. The set up had  
299 the added advantage of being very portable, completely removing sunlight and limiting dust  
300 exposure. We report XXX scans using the NextEngine Laser scanner.

301 Finally, hand samples were collected and analyzed with the Zygo blah blah, an optical  
302 profilometer enabling accuracy from millimeters down to sub-micron. The Zygo blah blah  
303 uses white light interferometry to produce relatively small point-clouds (XXX points) a various  
304 magnifications. It does however allow for seamless stitching of scans. Individual and stitched  
305 scans using the profilometer where benchmarked to a silicon carbide reference machined flat to  
306 XXX meters. All samples where scanned at 20x magnification and stitched together to produce  
307 sections roughly XXX by XXX millimeters. In additions, samples where scanned at the lowest  
308 magnification to properly bridge the gap up to the laser scanner resolution. We report scans

309 of XXX samples with the white light profilometer, XXX of which were taken from surfaces  
310 scanned in the field with the laser scanner.

### 311 3.2 Constraining displacement

312 We associate every scan with a displacement constraint. Field areas where specifically chosen  
313 for the exceptional exposure and relatively simple offset markers. For the Chimney Rock Fault  
314 Array and Big Hole Fault entire displacement profiles have been measured during previous  
315 detailed mapping campaigns (i.e. Maarten shipton). At Iron wash, Horse Creek and Molly's  
316 Castle, Atilla Aydin's mapping identified clear offset markers. Base maps for all these areas  
317 were georeferenced onto satellite images and used in the field to streamline data acquisition.  
318 Where fault exposure was good, we populated the maps with additional measurements using  
319 basic tape measure and compass triangulation methods.

320 It is important to recognize that the base maps only report stratigraphic throw or, in some  
321 cases, actual offset across *entire* fault zones. In the field we typically observe not one, but  
322 many slip surfaces along with very complex networks of deformation bands and sheared joints  
323 which partition displacement across many interfaces throughout the fault zone (see figure).  
324 In this study, we make a distinction between *offset* across the entire fault and *displacement*  
325 across a single fault slip surface. Without good marker horizons and cross-sectional exposure,  
326 determining how stratigraphic offset is accommodated across slip surfaces can be ambiguous,  
327 and thus requires detailed outcrop mapping (e.g. shipton ???) At Big Hole fault, two large-  
328 scale continuous strands of the fault, both accommodating meters of displacement exemplify this  
329 mechanism at a larger scale. In accordance, Shipton and Cowie, 2003 report large uncertainty on  
330 the partitioning of stratigraphic offset across the two strands. This implies that offset across the  
331 entire fault zone is an upper-bound constraint on displacement for a given slip surface. In XXX  
332 of XXX fault slip surface measurements, this is the best available constraint on displacement.

333 We were able to reconstruct exact displacement and offset partitioning where cross-sectional  
334 in the following specific cases: 1) If cross sectional exposure indicates that there is only a single  
335 slip surface; 2) If cross-sectional exposure is good enough to clearly indicate the fault trace, an  
336 offset marker (lamella, cross-bedding or lithological contact) and near enough to the slip surface  
337 exposure; or 3) if it is unambiguous that one slip surface is accommodating an overwhelming  
338 majority of displacement, i.e. it is continuous, it has a layer of fault rock and it distinctly more  
339 linear and sharp than any other slip surface in the fault zone.

340 While the latter does not preclude the possibility for displacements to be accommodated on  
341 other smaller slip surfaces, for larger displacement faults (more than 10 m of slip), these smaller  
342 displacements will not amount to a significant portion of the total slip. In detailed outcrop maps,  
343 Shipton showed that the displacement accommodated by small discontinuous slip surfaces was  
344 minimal compared that accommodated by an unambiguous large displacement strand, here on  
345 after referred to a *principle slip surface* (PSS).

346 Cases where a clear PSS is unambiguously identifiable allowed us to characteristically further  
347 criteria for a confident identification of a PSS for the Navajo and Entrada Sanstones as follows:

- 348 • *The PSS is an interface between two displaced fault blocks.* As such juxtaposition of two  
349 distinct rock types (e.g. distinct stratigraphic horizons and/or fault rock) by faulting is  
350 an unambiguous indicator;
- 351 • *the PSS has a distinctly sharp, continuous, relatively planar morphology in cross section.*  
352 A certain panarity must exist to prevent substantial geometric mismatch;
- 353 • *in line with the implicit definition of a fault, the PSS is nearly cohesionless.* Locations  
354 identified to be expose section of a PSS inevitably cracked open when sampling across the

355 slip surface—the slip surfaces had no cohesion. Cohesion is typically thought to reinstate  
356 by precipitation and healing. We did not observe recovered healing in this study.

- 357 • the PSS has a vitreous finish;
- 358 • The PSS is typically in the center of a damage zone. Damage is an inevitable conse-  
359 quence of displacement and the accompanying mismatch that accumulates. Damage at  
360 the field locations in this study is expressed as comminution (*e.g.* cataclasite and gouge),  
361 fragmentation (*e.g.* breccia, splay joints) and shear deformation (specifically deformation  
362 bands).

363 \*make a table regarding the different types of displacement constraints\*

364 known unknown equation assumptions N

365 - throw - assuming 60 deg dip, dip slip - throw, dip – assuming dip slip - throw, dip, rake –  
366 assuming constant displacement orientation - direct off-set – with different permutations ...

## 367 4 Scan data Processing

368 I use point cloud spatial statistics to characterize and quantify active surface processes on faults.

369 I developed a *MatLab* work flow to entirely automate data processing from the raw .xyz input  
370 format to the final statistical analysis:

### 371 1. Preprocessing

- 372 (a) manual inspection for coarsest defects
- 373 (b) Import .xyz data into *Matlab*
- 374 (c) Very coarse Height field filter
- 375 (d) Flatten points
- 376 (e) Grid data
- 377 (f) Orient grid along slip direction (using power spectral analysis)
- 378 (g) Remove defects
  - 379 i. Remove outliers in the height field
  - 380 ii. Fractal model filter
  - 381 iii. Remove abnormally flat (interpolated) sections

### 382 2. Processing

- 383 (a) Statistical analysis
  - 384 i. Scale dependent *RMS*
  - 385 ii. Scale dependent skewness
  - 386 iii. Scale dependent kurtosis
  - 387 iv. Scale dependent asymmetry
- 388 (b) Spectral Analysis
  - 389 i. Fast Fourier Transform (FFT)
  - 390 ii. Lomb-Scargle Periodogram

391        *make into figure, include bypasses and other recent additions*

392        Note that the general pre-processing workflow was slightly adapted according to the different  
393        instruments that where used in the study. These adaptation were mostly attributable to the quality  
394        of the data at the various scales of acquisition and the actual instrument specifications.  
395        Scans collected with the LiDAR required more extensive manual point removal to avoid features  
396        such as vegetation, spurious outlier and large defects to affect the quality of the preprocessing.  
397        Scans collected at the intermediate scale with the laser scanner easily followed this workflow.  
398        Finally, scan collected with the white light interferometer did required minimal preprocessing  
399        and where aligned manually at the time of data collection.

400        

## 4.1 Surface Pre-processing

401        Before conducting a statistical analysis scan data must be pre-processed into a workable format.  
402        Scan data is a point cloud - a series of points with coordinates  $x$ ,  $y$  and  $z$ . Scans reported in this  
403        study typically have  $10^6$  to  $10^7$  points. In raw form, the point clouds are randomly oriented,  
404        noisy and still contain instrumental and physical artefacts. Physical artefacts include cracks,  
405        eroded sections, and vegetation; instrumental artefacts include noise, smoothing and scattering.  
406        All these features must be removed. The process of manual removal is labour intensive and  
407        unfeasible for a data set of the scope presented in this study. I rather opt to automate this  
408        process. Only very large defects (defects that may substantially effect the quality of finding a  
409        true mean plane) are manually removed.

410        

### 4.1.1 Point Cloud orientation and Gridding

411        The surface must both be flattened and aligned along slip. Linear trends in the data induce an  
412        unwanted high frequency signal in data and also affect the quality of later interpolation onto  
413        a grid. Thus,  $x$ ,  $y$ ,  $z$  data is rotated using around the axis  $\mathbf{u}$  as determined by the normalized  
414        cross product between the surface normal  $\mathbf{n}$  and a vector normal to a flat surface ( $\mathbf{n}_2 = [001]$ ):

$$\mathbf{u} = \mathbf{n} \times \mathbf{n}_2 / |\mathbf{n} \times \mathbf{n}_2|$$

415        with the rotation,

$$R = \cos \theta \mathbf{I} + \sin \theta [\mathbf{u}]_x + (1 - \cos \theta) \mathbf{u} \otimes \mathbf{u},$$

416        where  $[\mathbf{u}]_x$  is the cross product matrix of  $\mathbf{u}$  and  $\otimes$  is the tensor product and  $I$  is the identity  
417        matrix.

418        Fault surfaces are anisotropic. The direction of slip is preserved in the anisotropy whereby  
419        the 'smoothest' direction is slip parallel and the 'roughnest' direction is perpendicular to slip.  
420        The fault scan is rotated around the  $z$  axis such that the direction of slip is along the  $x$  axis.  
421        The direction of slip is by decimating raw data before iteratd steps of regridding, one-degree  
422        rotation and spectral analysis. In the radial search, roughness is quanified as the integral  
423        of the log-weighted power spectrum over the entire bandwidth of the sample surface. The  
424        angle associated to the minimum in roughness is then identified as the direction of slip and  
425        subsequently used to rotated the original flattened point cloud. The data is then interpolated  
426        onto a grid using a linear interpolation algorithm. The point spacing is automatically defined  
427        by the point density over the areal extent of the data:

$$\Delta x = N_{pts} / AXXXXXX \quad (6)$$

428 **4.1.2 Surface Defect Removal**

429 INCLUDE HISTOGRAMS FOR EACH FILTER

430 *Defect* include all physical surface features that are clearly not associated any faulting  
431 process, *e.g.* cracks, eroded patches, vegetation, etc.. Defects are identified and filtered out  
432 using combination of thresholding methods. These methods all revolve around identifying clear  
433 points or segments that are statistical outliers to the distribution characterizing the entire  
434 surface—abnormal points.

435 The most aggressive filter implemented searches for outliers to the fractal model. The filter  
436 removes entire linear segments with abnormally high variance in the height field for the given  
437 scale of observation. For this implementation, I iterate over 10 filter scales. The scales are  
438 selected using a log spacing from the 10 points up to the length of the entire surface. The  
439 threshold for segment removal is chosen to be four standard deviations from the mean (should  
440 account for < 0.1 percent of the data in a normal distribution). Note that, assuming a normal  
441 distribution of variance data for a given scale, the filter should not induce a systematic bias since  
442 the filtering is symmetric around the mean. However, surface features associated with a truly  
443 distinct mechanism of formation, in this case cracks and other defects that will typically have  
444 much higher variance, *are* be removed. This general approach ensures that defects, regardless  
445 of their scale get identified and removed. This is important for any subsequent fractal analysis.

446 Abnormally flat sections arise as the result of triangular interpolation of sparse points.  
447 Typically, interpolation on the edge on a non-convex set of points is subject to this effect.  
448 These artefacts are readily identified in the curvature data. In the log-transformed absolute  
449 value curvature field, these sections appear to be nearly or exactly zero. The filter rejects  
450 point with curvatures less than  $10^{-25}$ . These values likely associated to the linear interpolation  
451 scheme.

452 Finally, all scans are inspected to make sure that the pre-processing was successful. The  
453 script fails to properly process scans that are excessively populated with surface defects. These  
454 scans were manually cleaned and oriented before re-processing them. Manual changes were  
455 executed in *CloudCompare*.

456 Pre-processed scans are  $N$  by  $M$  scalar fields of fault surface topography (the distance from  
457 the mean plane) aligned with slip along the  $x$  axis. NaN values mark locations where data is  
458 missing or was removed by filters. Point spacing is defined the mean point density of the scan  
459 in the  $x$ - $y$  plane.

460 **4.2 Statistical Analysis**

461 **4.2.1 Spectral Analysis**

462 **4.2.2 More Spatial Statistics**

463 INCLUDE A FIGURE WITH: ORIGINAL SURFACE, AUTOMATICALLY PROCESSED  
464 GRID, MANUALLY PROCESSED GRID AND CORRESPONDING POWER SPECTRA.

465 **5 Results**

466 **5.1 Observations**

Location	Lithology	Description	Displacement Constraints
Chimney Rock Fault Array	At the contact between the Navajo Sandstone and the base of the Carmel Unit	Orthorombic set of normal faults with preserved faults scarps of Navajo Sandstone	Displacement profiled of stratigraphic throw constrained by offset on a Carmel Limestone Marker Horizon by Maerten et al., 2000.
Big Hole Fault	Navajo Sandstone	One single large normal fault structure partitioning displacement on two major strands traceable for kilometers through a river wash with scarp exposure, and strike parallel/perpendicular cross-sectional exposure	Displacement constrained using the top Erosionally competent horizon at the top of the Navajo by Shipton and Cowie, 2003 and directly where possible.
Iron Wash	Navajo Sandstone	Network of normal and strike-slip cross-cutting faults. Little scarp exposure but has good cross-sectional exposure with fresh slip surfaces (using hammer and chisle)	Displacement mostly constrained by direct measurement of offset in the Upper Navajo horizon.
Molly's Castle	Entrada Sandstone	East-West striking network of normal faults and ubiquitous deformation bands. Well preserved slip surfaces broadly associated to a single slip surface structure intermittently bounding and crosscutting a thick (30 cm cluster of deformation bands	Displacement constraints available in places from mapping by Aydin (1978) and directly measured using various marker horizons within the Entrada Sandstone (e.g. laminae, cross-bedding unconformities, and thick red sandstone horizons depending on scale)

Table 1: Table caption

467

12

468

469 **5.2 Field observations and Microstructure**

470 The field observations and microstructures, in unison, build towards a qualitative characteri-  
471 zation of fault maturation. I report on the fault architecture in the Navajo and Entrada Sand-  
472 stones with a specific focus on the evolution from zero-displacement structures such as joints  
473 and deformation bands to large offset structures with polished slip surfaces and accompanying  
474 fault rock lithologies.

475 **5.2.1 Fault architecture**

476 Faults in the Navajo and Entrada sandstones generally record dip slip. Rotation of slip-direction  
477 is typically associated points where larger fault structures crosscut each other. The general ar-  
478 chitecture of the faults is complex. At all observable scales of observation, faults outcrop in  
479 relays and cross-cutting conjugate sets typically dipping at  $60^\circ$ . The PSS fault model is only  
480 rarely representative of the fault architecture. Fault zones rather have many slip surfaces,  
481 sheared joints and splays which partition offset. As is characteristic for high porosity sand-  
482 stone, fault zones all have deformation bands. The intensity of deformation bands decreases  
483 exponentially away from the center of the fault zone and was shown to correlate in intensity  
484 with displacement on the fault (cite someone). Deformation bands typically abut obliquely into  
485 the slip surfaces at shallow angles (less than  $70^\circ$ ). For an extensive review and description of  
486 the faults in the Navajo and Entrada sand stones refer to Aydin's thesis.

487 1 or 2 : Photo j-; sketch of a cross-section through typical fault architectures

488 **5.2.2 Zero-Displacement Structures**

489 Deformations bands and joints are a ubiquitous and characteristic feature around faults in high  
490 porosity sandstones. Larger fault structures nucleated from pre-existing networks of deforma-  
491 tion bands and joints ([?]???). Deformation localizes and intensifies along theses structures to  
492 then create through-going faults. The characteristics and surface morphology of these features  
493 are especially relevant to our analysis as they represent the 'primordial roughness' of faults.

494 *Deformation bands* are recognizable in outcrop as sinuous white bands, 1 to 5 millimeters  
495 in thickness, that accommodate shear offset. In sandstones, small strain can be mechanistically  
496 accommodated by the run-away collapse of grains in sub planar sheets [?] ??. In thinsection,  
497 ... The reduction of grain size and the associated compaction causes the deformation bands  
498 to be stronger and more resistant to erosion than the host sandstone [?]. Unlike slip surfaces in  
499 the area, deformation bands do not reduce the cohesion of the rock—they do not induce a well  
500 define parting surface. Deformation bands preferentially resist erosion, often causing them to  
501 protruded out of outcrops. *Deformation band clusters* accommodate more intense and localized  
502 shear strain. The clusters are dense networks of anastamozing deformation bands ranging from  
503 a few millimeters to tens of centimeters in thickness, often outcropping as slabs up to meters in  
504 sizes (especially in the Entrada Sandstone). In the extensional regimes presented in this study,  
505 clusters commonly form in upright conjugate pairs, each dipping  $60^\circ$ .

506 The edges of deformation band clusters that have eroded out appear to have a distinctly  
507 corrugated and "lumpy" morphology ( figure for this?). The orientation of the corrugations is  
508 in clear agreement with cross-sutting slip surfaces kinematic indicators. The slabs are coated  
509 with sand grains from the host sandstone. There is a clear directional asymmetry along the  
510 direction of shear (see figure 1). Larger clusters often have one or many through going slip  
511 surfaces. Cross cutting relationships along more mature fault structures show deformation  
512 bands both pre-dating and postdating the nucleation of the fault. (\*Probably need a figure for  
513 this\*). Please refer to Fossen, Shipton, Aydin for more detailed and extensive characterizations  
514 of defomation bands in these localities.

515 Pre-existing regional joints sets are a common feature of every locality. Joints typically  
516 have dips near  $90^\circ$ . Joints set are most readily measurable in the upper Navajo units and low  
517 Carmel limestone pavements. The intensity of joint increases near the fault with the occurrence  
518 of syn-kinematic sheared and splay joints. Refer to Aydin and Davatzes for extensive analysis  
519 of joint characteristics and relative timing for each locality.

520 Systematic associations between the type and abundance of The Entrada unit is has more  
521 deformation bands and fewer and less well defined joints. Moreover, in the Chimney Rock fault  
522 array, there is a clear association to the conjugate fault set orientation. Faults striking



Figure 1: Left: Example of the edge of a deformation bands cluster at Molly's Castle. Note the "lumpy" morphology and an clear vertical directional asymmetry. Right: Cross-sectional view of a deformation band cluster with tens of centimeters of shear offset. It is unclear weather there is a through going slip surface localizing displacement. It is , however, definitely not on the edge of the cluster.

### 523 5.2.3 Slip Surfaces

524 Slip surfaces in the Navajo and Entrada sandstones are most readily identifiable by their vitreous  
525 polish. Striations, grooves and mullions mark the direction of slip. In Cross-section slip surfaces  
526 are sharp, smooth relative to their zero-displacement counterparts, and milky white with the  
527 notable exception of the north fault in the chimney rock fault array, where well-preserved slip  
528 surfaces had a distinct dark grey color. The slip surfaces often crosscut or bound deformation  
529 band clusters. Slip perpendicular profiles are notably more sinuous than in the slip parallel  
530 direction. Slip surfaces are only preserved in the Navajo and Entrada Sandstones. In spite of  
531 good exposures in prospecting pits and careful inspection of the slip zone, the Navajo-Carmel  
532 contact at the Chimney Rock fault array did not preserve good surfaces in the Carmel Unit.  
533 It is unclear whether this indicates that the Carmel units is more susceptible to erosion and/or  
534 alteration; or if a polished finish is only a feature of the quartzite sandstones. Pristine fault  
535 slip surfaces are not cohesive, and always act as a parting surface. Slip surfaces uncovered *in*  
536 *situ* using a hammer and chisel reveals a relatively consistent meso-scastructure (see figure –  
537 figure similar to that in Jamies notes), A sharp interface, separated by a sub-mm thick layer of  
538 incohesive white powder bounded by two vitreous surfaces is a dense set of deformation bands.

539 Surfaces that are notably more eroded and indurated have a reddish-brown to dark tarnish  
540 and can loose their vitreous luster. Sections of the slip surface are plucked off. Severely  
541 wethered scarps, not scanned in this study, develop a slip perpendicular fabric associated to  
542 conjugate fractures and deformation bands abutting into the slip surfaces. We can confidently  
543 attribute these effects to erosion because they did not occur in freshly parted slip surfaces and  
544 appeared to have systematic association to sun exposure. Lichen grew preferentially on north  
545 facing scarps. From our field observation, it is clear that erosion has the effect of re-roughening



Figure 2: Left: Example of at least two distinct polished slip surfaces on the same fault structure. Right: Example of concentric pattern on cross-sectional view a fault

546 the slip surfaces, especially at smaller scales. How the roughening process scales is, however,  
547 unclear from our field observations.

548 In thin section...

549 Faults with small displacements on the order of millimeters to centimeters are distinctly  
550 different than larger displacement faults. Smaller displacement faults are visibly more sinuous,  
551 laterally discontinuous and less polished. They do not have well-defined gouge or cataclasites  
552 layers bounding the slip surface. In spite of extensive investigation, we do not observe faults  
553 with well-defined slip surfaces with clear offset markers indicating less than approximately half  
554 a centimeter of displacement.

555 Microstructurally... (thin section + SEM pics)

#### 556 5.2.4 Fault Rock

557 In this study, we refer to *fault rock* as rock altered either mechanically or chemically by the  
558 influence of the fault. The faults in our study area display a very diverse range in fault rock  
559 lithologies, ranging from fine-grained cataclasites to massive bodies of breccias (up to meters of  
560 thickness). Fault rock consistently bounds slip surfaces—often asymmetrically. However, both  
561 the lithology and thickness of the fault rock are highly heterogeneous and are subject to drastic  
562 changes at the outcrop scale (10's of meters) both along the strike and dip. We pay careful  
563 attention to the fault rock as it is inevitably coupled to the slip surface roughness and its  
564 maturation with cumulative displacement.

565 Healed Gouges - the spot at big hole - iron wash (powder between the surface) - micro-  
566 structure - prospecting pit - typically on thinned sections of the fault rock (near the slip  
567 surface) Cataclasites . . . - big hole sample with slip surfaces on both sides of the cataclasite -  
568 micro-structure - Breccias . . . - thick sections of the Breccias occur lenses which range from cm's  
569 to meters in thickness. Breccia clasts are typically poorly sorted and can be very coarse with  
570 clast up to 10 cm in diameter. Clasts show indications for multiple generations of brecciation.

571 Thin Quarts lens - iron wash

572 Systematic associations between fault rock and fault structure exist. For instance, Davatzes  
573 et al., 2002 reports of a systematic association between the fault rock lithology and the ori-  
574 entation of the fault set. Namely, the orthorhombic fault set striking WNW has systematic  
575 association with fragmentation—fault breccias; conversely the ENE fault set rather has slip sur-  
576 faces cutting through deformation band clusters (see figure ??). This relation was speculated to  
577 be the result of contrasting genetic mechanism. The WNW set is the result of the reactivation  
578 of regional joints. In contrast the ENE fault set is the the result of clustering and anastamosing  
579 deformation bands acting as a catalysing agent to the formation of a faults. In this study, we

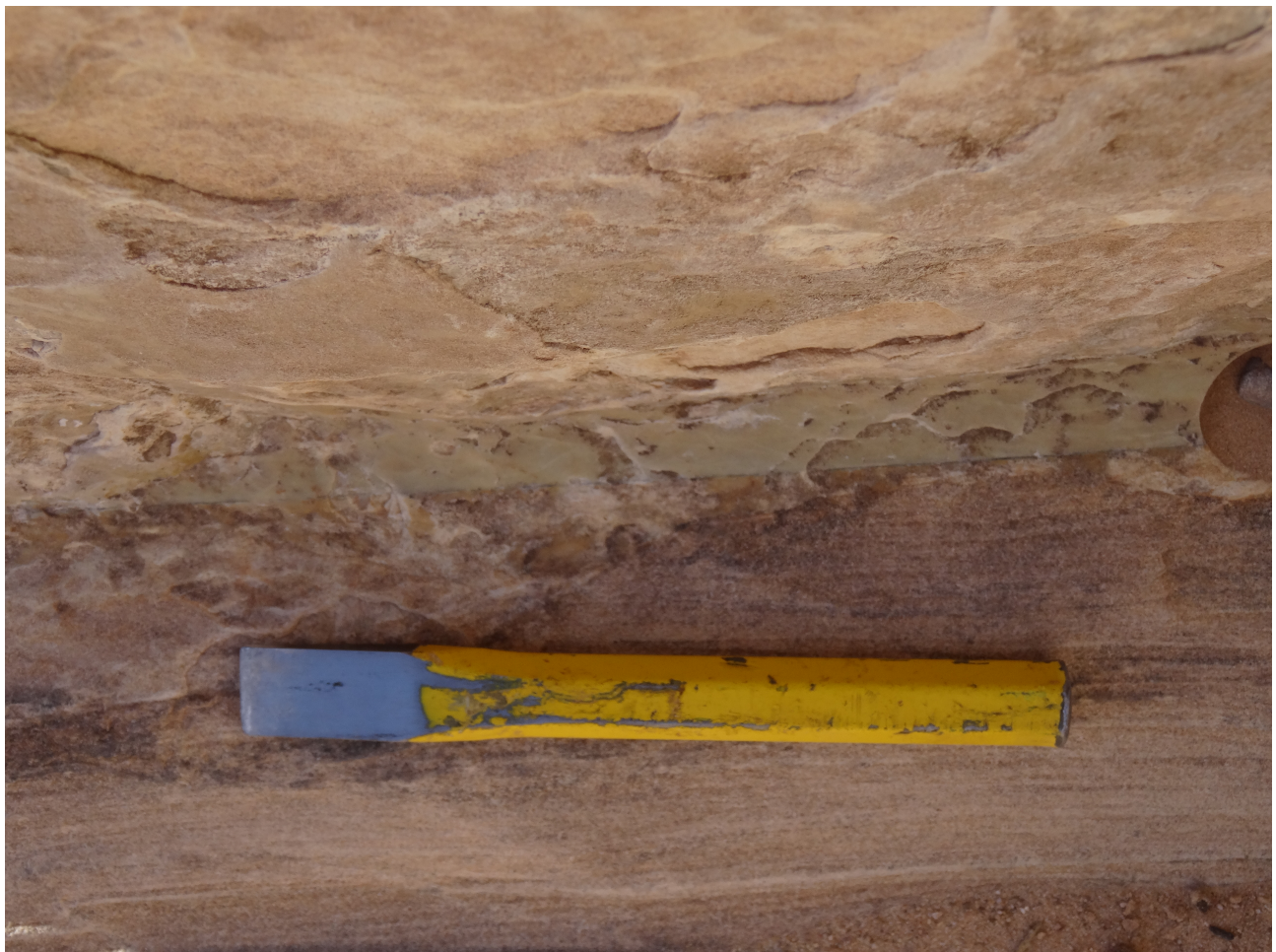


Figure 3: Example of a slip surface interpreted as a principle slip surface with around 20 meters of displacement at Big Hole Fault

580 observe clear instance of lithological contacts being associated to brecciation (photo at iron  
581 wash where the top of the Navajo is brecciated and quickly reverts to a single fault strand.  
582 More over, large breccia bodies are clearly related to points where faults are cross-cutting each  
583 other at high obliquity as is often the case at the Chimney Rock fault array and  
584 Complicating factors:  
585 Associations between brecciation and lithological contacts...  
586 Associations between brecciation and cross cutting faults...

## 587 **5.3 Roughness measurements**

588 figures to include:

- 589 • all spectra  
590 • increasing anisotropy (two surfaces) - polar plot

### 591 **5.3.1 Lidar**

592 qualitative illustration of maturity

### 593 **5.3.2 Laser scanner**

### 594 **5.3.3 White light**

## 595 **6 Interpretation of field observations and roughness 596 measurements**

## 597 **7 Model**

### 598 **7.1 Modelling Objectives**

### 599 **7.2 Model Outline**

600 In this study, we utilize work minimization numerical modelling to capture the growth  
601 of fault damage and the effect of rough asperities. The models are built off of fric2d  
602 and growth by optimization of work (GROW) developed by Michele Cooke and Jessica  
603 McBeck.

#### 604 **7.2.1 GROW**

605 Growth by optimization of work predicts fracture propagation paths. It does so by mini-  
606 mizing the external work on the system. The model theoretically allows for the simulta-  
607 neous growth of multiple fractures and

608 The general algorithm uses a boundary element method to describe the fractures-linear  
609 dislocation elements that discretize the entire length of the fault. As a crack grows,  
610 dislocation elements are added radially to the tip of the crack so as to minimize the

611 external work on the system normalized by the crack area ( $W_{ext}/\Delta A$ ). External work is  
 612 further defined as:

$$W_{ext} = \oint (\tau u_s + \sigma_n u_n) dB \quad (7)$$

## 613 7.3 Model Results

# 614 8 Discussion

### 615 8.0.1 Tying the model together with roughness measurements and model 616 wear rate (character), tying together model with

## 617 8.1 An external estimate of gouge production and fault thickness

619 The data collected in this study offers the unique opportunity to provide new indirect  
 620 estimates of fault rock production, fault thickness and dilation rate over an entire fault.  
 621 We know that 1) the primordial roughness is systematically rougher than mature faults,  
 622 2) the primordial roughnes is relatively constant, and 3) the roughness can be estimated  
 623 for a given displacement. Using these results, I will estimate the volume of fault rock  
 624 produced through wear and the corresponding roughness induced accomodation space in  
 625 the fault system.

626 Displacing two rough fractal surface in shear requires dilation. The expectation dilation  
 627 can be estimated according to the amplitude of the largest wavelength ( $\lambda$ ) being offset  
 628 (see figure XXX). For a given displacement,  $u$ , the largest wavelength in the system  
 629 will be  $\lambda = 2u_i$ . Using a fractal paradigm to define the average amplitude of a given  
 630 wavelength according to the pre-factor  $\beta$  and the Hurst scaling exponent,  $H$ , (\*reference  
 631 the equation\*) we find that the dilation,  $A$  can be expressed as a function of displacement:

$$A(u) = \sqrt{\beta 2u^{-2H-1}} \quad (8)$$

632 If we apply this to an entire fault system with displacement field,  $U$ , we can estimate the  
 633 void space that would be produced:

$$V_{void}(U) = \int_S \sqrt{\beta 2U^{-2H-1}} dS \quad (9)$$

634 Since the fault system is closed any change in fault roughness *must* be coupled to the fault  
 635 core. If all changes in the fault surface are associated to a production of fault rock, we can  
 636 effectively estimate the volume of fault rock that has been produced from diplacement  
 637  $u_0$  to  $u_f$  by comparing the volume integral under the corresponding initial and final slip  
 638 surfaces  $S(u_0)$  and  $S(u_f)$ .

$$\frac{\Delta V_{faultrock}}{\Delta u} = \int_S S(u_0) - S(u_f) dS \quad (10)$$

639 volume integral under the surfaces,  $S$ , can be estimated numerically according to the  
 640 frequency distribution prescribed by the RMS the entire fault system. Note that the

641 RMS is estimated at the length scale of the entire fault; wear processes are active at all  
642 length scales below this.

$$\int S dS \approx \quad (11)$$

643 Now for the displacement field,  $U$ , we can estimate the total fault rock produced by  
644 using the primordial surface roughness,  $S(0)$ , and the prediction of the surface roughness  
645 extrapolated to the length of the fault (\* reference the the equation of smoothing \*) such  
646 that:

$$V_{faultrock}(U) = \int_S S(0) - S(U) dS \quad (12)$$

647 The comparison between the two quatities is telling. If the amount of fault rock is

## 648 9 conclusion

### 649 9.1 future work

## 650 10 Appendix

### 651 10.1 Surface Processing scripts

652 Or possibly a link to a git repository...

### 653 10.2 User manual for script

654 This manual should serve as both a basic guide to the logic and usage of the *surface*  
655 *processing package*.

656 The master function of the package is *surfaceprocessing*. This function effectively deal  
657 with the inputs and direct computations towards the necessary functions. Outputs of  
658 the function are a .mat workspace file for each input data file. The workspace includes  
659 a structure (called *parameters*) with the raw surface analysis outputs, the point spacing,  
660 the decimation factor (if any), the file name and the date of the analysis. The workspace  
661 also includes the grid form of the original inputed surface (called *surface*), and the pre-  
662 processed copy that was used for the subsequent analysis (called *zGrid*). Inputs are always  
663 included in pairs. The former defines the type of input, the latter qualifies or quantifies  
664 the input. This structure allows for adaptability of the code to various needs. Options  
665 include the following:

- 666 – *what to do?*: 'toDo', followed by the desired analyses on of: 'FFT', 'PLOMB', 'pa-  
667 rameters' or 'all' (default is 'all') - can be a cell array. This specifies what kind  
668 of spatial analysis will be done on the input surface data. The spatial analysis is  
669 calculated and averaged across every single profiles along the surface. The analyses  
670 are the following:
  - 671 \* 'FFT', a power spectrum computed using a Fast Fourier Transform (FFT) al-  
672 gorithm;

- 673                   \* 'PLOMB', a power spectrum computed using a least-squares Lomb-Scargle al-  
 674                   gorithm;  
 675                   \* 'paramters', the calculation (as a function of scale) of the Root Mean Squared  
 676                   (RMS), skewness, kurtosis and asymmetry averaged across all segments of a  
 677                   given length on all profiles of the surface.  
 678                   'all' simply performs all the analyses outlined above.  
 679                   – *skip pre-processing?*: 'bypass', followed by 'zygo', 'pre-processing' or 'no' to be used  
 680                   input is already in aligned clean grid form - input files are then (default is 'no').  
 681                   'zygo' is specifically adapted to the proprietary data format of the white light in  
 682                   Wong. 'pre-processing' simply skips any pre-processing. This option requires a  
 683                   .mat structure with a field named 'grid' with the topography and a field name  
 684                   'pointSpacing' specifying the point spacing (in meters). In either case the topography  
 685                   must be aligned such that the positive x direction is the parallel direction.  
 686                   – *for the parameter analysis, how many scales?* 'numberOfScales' followed by the  
 687                   desired number of analysed scales. This option is relevant to the parameters analysis.  
 688                   Note that this has a lot of effect on the amount of processing time (default is 10).  
 689                   – *decimation*: 'decimationFactor' followed by the desired decimation factor (default is  
 690                   1). Decimation is a useful tool to reduce computation time. The surface grid is sub-  
 691                   sampled according to the decimation such that a decimation factor of  $k$  would imply  
 692                   that only every  $k$ th point on the every  $k$ th will be considered for hte subsequent  
 693                   analysis.  
 694                   – *Instrument specific analysis* 'instrument' followed by 'white light', 'laser scanner' or  
 695                   'lidar' (default does not set any instrument specific adjustments). Some instrument  
 696                   specific pre-processing steps are taken. Please contact me if you intend to use this  
 697                   as they may be highly dependent on the specific instrument used.

698                   For instance, *surfaceprocessing('todo','FFT','bypass','zygo')* will only perform a power  
 699                   spectral density analysis and will skip preprocessing and assume that all input will be in  
 700                   the 'zygo' export .xyz format.

701                   When the command is executed, the user will be prompted to navigate to the directory  
 702                   where the input data is located. IMPORTANT: the directory must *only* contain files of  
 703                   one data format. There cannot be other files or sub-directories in the directory. The user  
 704                   will then be prompted to choose a destination for the output data. The requirements  
 705                   for the output location are less stringent. However, it is advisable to choose an empty  
 706                   directory such as to facilitate subsequent steps.

707                   The next step is to visualize the output of the analysis. This is done using the *unpack*  
 708                   *parameters* function. This function provides various visualization options for all files in  
 709                   the directory chosen by the user. The first input (the *desired plot*) can be one of the  
 710                   following:

- 711                   'FFT': plot all power spectra;  
 712                   'PLOMB': periodogram plot as determined by the Lomb-Scargle least squares anal-  
 713                   ysis;  
 714                   'topostd': plot of the root mean squared (RMS) as a function of scale;  
 715                   'topoSkew': plot of skewness of height fields as a function of segment scale;  
 716                   'topoKurt': plot of the the kurtoisis of height fields as a function of segment scale;

717       'PowerVsDisp': plot of power interpolated at a given scale as a function of displacement;  
718  
719       'RMSVsDisp': model RMS at a given scale as a function of displacement  
720  
721       'Grids': shows both the original and pre-processed grid for the specified file 'file-  
Name';  
722  
723       'Best Fits': best logarithmic fits to power spectra obtained from the fast fourier  
transform analysis.

724 The functionality of the packages is broadly divided into three sections: 1) importing and  
725 preprocessing data, 2) performing various spatial statistics on the pre-processed data, and  
726 3) unpacking the analysis output into figures.

727 In order to run smoothly the all functions included in the package should be kept in the  
728 same directory or on an accessible path.

729 For reference, here is a quick outline of what each function does:

730       *affine fit*: (from mathworks) Computes the plane of best fit using least squares  
731       normal distance;  
732       *align grid*: finds the smoothest directions in a grid using FFT spectra and rotates  
733       and re-grids the input grid;  
734       *fault spectral density simple*: Calculates the average lomb-scargle spectral density  
735       every row of a N by M array;  
736       *FindErr loop anisotropy*  
737       *flatten XYZ*: removes planar trends from XYZ data by applying a rotations matrix  
738       according to the best fit plane (*affine fit*);  
739       *fractal model outlier*: Removes outlying segments according to a near-gaussian model  
740       for the distribution of RMS values at specified segment lengths (or scales);  
741       *frequency spectrum*: Calculates the average lomb-scargle spectral density of all con-  
742       tinuous segments on every single row of a N by M array;  
743       *parse zygo format*: extracts the both the point spacing and topographic grid from  
744       the exported zygo format. Can also remove planar trend from data (substracted  
745       from grid);  
746       *rotateZ*: applies rotation matrix on XYZ data  
747       *surface analysis*: Aggregates the analysis functions and applies them to an input  
748       grid  
749       *surface cleaning*: removes outliers associated to surface defects  
750       *surface parameters*: calculates spatial statistics and parameters along segments as a  
751       function of scale (RMS, skewness, directional asymmetry and kurtosis)  
752       *surface preprocessing 2*: deals with preprocessing input data (import data, cleaning  
753       and gridding data)